

Molecular-dynamics study of diffusional creep in uranium mononitride

Mohamed AbdulHameed^a, Benjamin Beeler^{a,b,*}, Conor O.T. Galvin^d, Michael W.D. Cooper^d, Nermene Elamrawy^a, Antoine Claisse^c

^a*Department of Nuclear Engineering, North Carolina State University, Raleigh, NC 27695*

^b*Idaho National Laboratory, Idaho Falls, ID 83415*

^c*Westinghouse Electric Sweden, Västerås, SE 72163, Sweden*

^d*Los Alamos National Laboratory, Los Alamos, NM 87545*

Abstract

Uranium mononitride (UN) is a promising advanced nuclear fuel due to its high thermal conductivity and high fissile density. Yet, many aspects of its mechanical behavior and microstructural features are currently unknown. In this paper, molecular dynamics (MD) simulations are used to study UN's diffusional creep. Nanometer-sized polycrystals are used to simulate diffusional creep and to calculate an effective GB width. It is found that Nabarro-Herring creep is not dominant in the temperature range of 1700–2000 K and that the dominant diffusional creep mechanism is Coble creep with an activation energy of 2.28 ± 0.09 eV. A method is proposed to calculate the diffusional GB width and its temperature dependence in polycrystals. The effective GB width of UN is calculated as 2.69 ± 0.08 nm. This value fits very well with the prefactor of the phenomenological Coble creep formula. It is demonstrated that the most comprehensive thermal creep model for UN can be represented as the combination of our Coble creep model and the dislocation creep model proposed by Hayes *et al.*

Keywords: Uranium nitride, Molecular dynamics, Coble creep, Nabarro-Herring creep, Grain-boundary width, Grain-boundary diffusion

*Corresponding author

Email address: bwbeeler@ncsu.edu (Benjamin Beeler)

1 1. Introduction

Uranium mononitride (UN) is a potential next-generation nuclear fuel with several favorable properties like high fissile density, good heat transfer, compatibility with most potential cladding materials, and longer fuel residence periods [1–3]. However, it also has challenges like complex manufacturing processes, high cost due to ^{15}N enrichment, and vulnerability to steam at high temperatures [1–3]. Many aspects of the mechanical behavior and microstructural features of UN at high temperatures and under irradiation are lacking in both consistent experimental data and detailed mechanistic understanding. The mechanical properties of nuclear fuels are crucial for a better understanding of the pellet-cladding mechanical interactions (PCMI) that occur during reactor operation, where cladding creep-down and fuel swelling lead to contact and the development of stresses between the cladding and the fuel, which, with the build-up of fission products, promotes stress corrosion cracking in the cladding material [4]. Fuel creep has an important role in accommodating void swelling once the fuel contacts the cladding [2].

There are a limited number of experimental investigations into the creep behavior of UN. Hayes *et al.* [5] developed an empirical correlation for the steady-state thermal creep rate of UN based on three experimental investigations by Fassler *et al.* [6], Vandervoort *et al.* [7], and Uchida and Ichikawa [8]. These experiments were conducted at a temperature range of 1373–2083 K, a stress range of 13–55.1 MPa, and for five grain sizes: 9, 15, 30, 140, and 2000 μm . In addition, the tested samples contained varying levels of carbon and oxygen impurities. To determine the mechanism controlling the creep of UN, Hayes *et al.* [5] determined the average stress exponent, based only on the data by Fassler *et al.* [6] and Vandervoort *et al.* [7], to be $n = 4.5$. They therefore concluded that the dominant creep mechanism is most probably a climb-controlled dislocation glide mechanism, for which there is no grain size dependence, i.e., the grain size exponent $q = 0$. The data by Uchida and Ichikawa [8] gave a stress exponent $n = 1.8\text{--}2.6$, which is indicative of a combination between diffusional and dislocation creep. However, Hayes *et al.* decided to disregard this data set because its temperature range was intermediate between that of Fassler *et al.* [6] and Vandervoort *et al.* [7], and they deemed it was unlikely that a diffusion-based mechanism would only be active in such a narrow temperature range (i.e., 1583–1773 K). The rest of the correlation (i.e., the prefactor and the activation energy) was only fit to the data by Vandervoort *et al.* [7] because it is the only data set that reported stoichiometric samples of 100% theoretical density. The final correlation reads:

$$\dot{\epsilon} = 2.054 \times 10^{-3} \sigma^{4.5} \exp\left(-\frac{39369.5}{T}\right), \quad (1)$$

where $\dot{\epsilon}$ is the creep rate measured in s^{-1} , σ is the stress measured in MPa, and T is the temperature measured in K. The correlation is strictly valid for $T = 1770\text{--}2083$ K (although it was assumed by Hayes *et al.* to yield reasonable estimates of the creep rate over the range of 298–2523 K), $\sigma = 20\text{--}34$ MPa, and theoretically dense UN. The exponential term in Eq. (1) corresponds to an activation energy $Q = 3.39$ eV.

Rogozkin *et al.* [9] performed experiments and reported thermal creep data for $\text{U}_{0.8}\text{Pu}_{0.2}\text{N}$. They found that for theoretically dense samples, the thermal creep rate follows the corre-

41 tion:

$$\dot{\epsilon} = 27.7\sigma^{1.35} \exp\left(-\frac{40000}{T}\right), \quad (2)$$

42 which indicates an activation energy $Q = 3.45$ eV. The investigators noted that the mass
43 fraction of oxygen and carbon impurities did not exceed 0.15% and the stress varied from
44 10 to 60 MPa. However, they did not report any grain sizes or an explicit unit for the
45 creep rate. Note that a stress exponent of 1.35 in Eq. (2) is close to 1 and might indicate a
46 diffusion-dominant creep mechanism [9, 10].

47 Nabarro-Herring (N-H) creep of UN has been investigated via computational tools. Ko-
48 tomin *et al.* [11] conducted a DFT investigation of the diffusion mechanisms of U and N
49 atoms in UN and calculated their associated migration energies. Assuming thermal creep
50 is rate-limited by the diffusion of the slower species (i.e., uranium), they concluded that
51 the activation energy of thermal creep in bulk UN is 5.6 eV. Their thermal creep model is
52 incorporated into the TRANSURANUS fuel performance code [11].

53 Finally, Konovalov *et al.* [12] conducted a compilation of available data on UN, (U, Pu)N,
54 UC, and mononitrides of refractory metals (e.g., Zr and Ti) to find a correlation for thermal
55 and irradiation creep in UN and (U, Pu)N. Based on the data, they assumed a combination
56 of dislocation-climb creep and Coble creep according to:

$$\dot{\epsilon} = a_1\sigma^n \exp\left(-\frac{Q_b}{k_B T}\right) + fa_2 \frac{\sigma}{k_B T} \exp\left(-\frac{Q_{GB}}{k_B T}\right), \quad (3)$$

57 where a_1 and a_2 are estimated from typical values for refractory-metal mononitrides, the
58 stress exponent of the dislocation-climb creep part is $n = 4.5$, the same as in Eq. (1), and
59 f is the volume fraction of GBs. Note that the dependence of the Coble creep on the grain
60 size is included in a_2 . They further assumed that the activation energy for the dislocation-
61 climb creep is equal to the activation energy of bulk diffusion of U atoms in UN, i.e., $Q_b =$
62 5 eV. Based on the observation that in typical metallic compounds, the activation energy
63 of GB diffusion is nearly half that of bulk diffusion, they assumed $Q_{GB} = 0.53Q_b$, similar
64 to UC, because measurements of U self-diffusion at GBs in UN are not yet available. An
65 important result of their analysis is that diffusional creep is the dominant mechanism in the
66 temperature range of fuel manufacturing processes and nuclear reactor operation, although
67 they did not clarify the effect of stress and grain size.

68 A few observations can be made about the previous studies. The assumption by Hayes
69 *et al.* that dislocation creep is the dominant creep process cannot be made for all grain sizes
70 at all temperatures based only on very few experimental data points. The studies by Fassler
71 *et al.* [6] and Vandervoort *et al.* [7], on which the stress exponent in Eq. (1) was based,
72 report grain sizes of 30, 140, and 2000 μm . However, typical grain sizes of manufactured
73 UN fuel range between 5 and 30 μm [13–16]. Johnson and Lopes [14] report that the grain
74 size for UN to achieve optimum fuel porosity (i.e., 0% open porosity to suppress oxidation
75 and 4% closed porosity to accommodate gas fission products) is around $8 \pm 1 \mu\text{m}$. Uchida
76 and Ichikawa [8], who found a stress exponent closer to 1, reported grain sizes of 9 and
77 15 μm . That is, diffusional creep might be the dominant creep mechanism at the grain
78 sizes typical of the manufactured fuel. The existence of diffusional creep as a contributing
79 process is supported by the studies of Rogozkin *et al.* [9] and Konovalov *et al.* [12], and can

80 be dominant if the activation energy of a diffusional creep mechanism is found to be lower
81 than that of dislocation creep. Basing the thermal creep model of UN on bulk diffusion
82 activation energies, as was done by Kotomin *et al.* [11], is questionable, especially because
83 GB diffusion is known to be much faster than bulk diffusion [17], and the typical grain sizes of
84 manufactured UN (5–30 μm) are quite small and might render Coble creep as the dominant
85 mechanism at the temperature range of practical interest. Finally, Nabarro-Herring creep is
86 expected to be dominant near the melting point [18].

87 It is worth mentioning that Hayes *et al.* [19] also developed correlations for diffusion in
88 UN based on a few scattered data points. Their estimated activation energies for U and N
89 atoms are 0.69 and 1.66 eV, respectively, which raises suspicions because U atoms are not
90 expected to have a lower diffusion activation energy than that of N atoms. Hayes *et al.*
91 reported that their correlation for N diffusion is for tracer diffusion measurements, and is
92 only representative of extremely hyper-stoichiometric conditions. Finally, while the analysis
93 by Konovalov *et al.* [12] is qualitatively appealing, it lacks quantitative insights because
94 it is based on typical values and educated guesses. In summary, the literature on creep in
95 UN is sparse, somewhat contradictory, and requires additional investigation to identify the
96 dominant creep mechanisms at various temperatures, stresses, and grain sizes.

97 Molecular-dynamics (MD) studies have been used with success to study diffusional creep
98 in, e.g., Si [20], Pd [21], and UO_2 [22, 23]. These studies set up a simulation for idealized
99 microstructures, where the supercells are equilibrated at a certain temperature and put
100 under stress, and the strain rate is then analyzed. Haslam *et al.* [24] further developed this
101 approach by using random grain sizes and shapes, instead of idealized microstructures, to
102 observe both creep rate and grain growth mechanisms in Pd. Cooper *et al.* [25] used another
103 approach (hereafter termed the parameter-based approach) for predicting Coble creep rates
104 for U_3Si_2 where, instead of directly observing creep, an initial creep formula is assumed, and
105 then, a lower-length scale modeling approach is used to calculate the formula parameters,
106 e.g., defect volumes and GB diffusivities. To the best of our knowledge, no computational
107 studies exist in the literature for Coble creep in UN.

108 In order to conduct MD simulations, a sufficiently accurate interatomic potential is re-
109 quired. Two promising interatomic potentials of UN exist in the literature: Tseplyaev and
110 Starikov's angular-dependent potential [26], and Kocevski *et al.*'s embedded-atom method
111 (EAM) potential [27]. Both potentials have been utilized and compared in our previous
112 works [28, 29], however, their ability to model dynamical processes like diffusional creep has
113 not been assessed. In this work, nano-sized polycrystals are employed to perform MD simu-
114 lations of diffusional creep in UN. The polycrystals are also used to study GB diffusion and
115 the temperature dependence of the diffusional GB width in UN. A parameter-based model
116 of Coble creep is also constructed and compared to the simulation model.

117 2. Methods

118 All MD calculations performed in this work utilize the Large-scale Atomic/Molecular
119 Massively Parallel Simulator (LAMMPS) software package [30] using a 1 fs time step and
120 the Tseplyaev [26] and Kocevski [27] force-field potentials. Periodic boundary conditions
121 (PBCs) are applied to all supercells. The Atomsk code [31] is used to generate polycrystals

122 by the Voronoi tessellation method. The OVITO software package [32] is used for supercell
123 visualization and analysis.

124 *2.1. Creep mechanisms*

125 Steady-state creep strain rates can be represented by the Mukherjee-Bird-Dorn equation
126 [33]:

$$\dot{\epsilon} = \frac{A}{T} \frac{\sigma^n}{d^q} \exp\left(-\frac{Q}{k_B T}\right) \approx C \frac{\sigma^n}{d^q} \exp\left(-\frac{Q}{k_B T}\right), \quad (4)$$

127 where T is temperature, σ is stress, d is the grain size, Q is an activation energy, k_B is the
128 Boltzmann constant, and A , n , and q are dimensionless constants. The inverse temperature
129 dependence A/T is relatively weak, especially at temperatures where creep is important,
130 and is usually neglected [34]. That is why $A/T \approx C$ is treated as a constant prefactor. The
131 values of the exponents n and q depend on the creep mechanism under consideration. For
132 example, for power-law (dislocation) creep, $n = 3-8$ and $q = 0$, i.e., no grain size dependence,
133 whereas for diffusional creep, $n = 1$ and $q = 2$ (for the Nabarro-Herring mechanism) or $q =$
134 3 (for the Coble mechanism).

135 It should be noted that the Harper-Dorn creep, a dislocation creep mechanism, has a
136 stress exponent $n = 1$, similar to diffusional-creep mechanisms, as well as $q = 0$, i.e., no
137 grain size dependence. However, for Harper-Dorn creep to be significant, the material must
138 have a large grain size (in the order of $100 \mu\text{m}$ [10]); otherwise, diffusional creep mechanisms
139 are more likely to dominate. There is little evidence for the existence of Harper-Dorn creep in
140 ceramics [10]. Ceramics generally have smaller grain sizes, fewer available slip systems, and
141 high Peierls-Nabarro stresses, all of which lead to the prevalence of other creep mechanisms
142 [10]. For this reason, the Harper-Dorn creep is excluded from consideration as a competing
143 creep mechanism in UN, and dislocation creep refers exclusively to power-law creep.

144 In this work, we study diffusional creep, whose rate, in general, is a sum of the Nabarro-
145 Herring creep rate, $\dot{\epsilon}_{\text{NH}}$, and the Coble creep rate, $\dot{\epsilon}_C$, since both mechanisms operate in
146 parallel [18].

147 For Coble creep, the steady-state strain rate is expressed as [18, 35]:

$$\dot{\epsilon}_C = A_C \frac{\sigma \Omega}{k_B T} \frac{D_{\text{GB}} \delta}{d^3} \quad (5)$$

148 where A_C depends on the grain shape ($A_C = 46.347$ for spherical grains), D_{GB} is the *effective*
149 GB diffusivity, δ is the GB width, and Ω is the vacancy volume usually approximated as
150 the atomic volume or expressed as b^3 [33] or $0.7b^3$ [10] where b is the magnitude of the
151 Burgers vector. In this formulation, $D_{\text{GB}} \delta$ is the diffusion flux in the GB, and $\sigma \Omega$ is the
152 work performed by the stress during an elementary diffusion jump [20, 21]. It should be
153 noted that the original paper by Coble [35] reports the value of A_C for spherical grains as
154 148. However, we performed the derivation by Coble and found a value of $A_C = 46.347$.
155 This agrees with the values of 47 reported by Kebinski *et al.* [20] and $148/\pi$ by Wang *et al.*
156 [36]. The maximum difference between these different results for A_C is only a factor of three;
157 thus, it is effectively negligible compared to the orders of magnitude difference in creep rate
158 resulting from, for example, d in Eq. (5). In Section 3.2, Eq. (5) is used as a basis for the
159 parameter-based Coble creep model.

160 Homogeneous grain elongation along the tensile stress direction during diffusional creep
161 requires GB sliding as a geometrically necessary accommodation process [18, 21]. In this
162 context, GB sliding happens sequentially to diffusional creep on a local atom-by-atom basis
163 and does not involve changes in the relative positions of the centers of mass of individual
164 grains (i.e., their coordinates normalized by the simulation box dimensions are constant)
165 [18]. If GB sliding were absent, voids/microcracks would form along the GBs. Since GB
166 sliding and diffusional creep occur sequentially and sliding is faster than diffusion [18], the
167 net creep rate is the rate of the slower process, which is diffusional creep.

168 *2.2. Diffusional creep*

169 High-temperature deformation and grain growth are coupled phenomena. Deformation
170 enhances grain growth, and, in turn, grain growth can either *increase* or *decrease* the defor-
171 mation rate depending on the interplay between the GB processes governing this coupling,
172 which include GB diffusion, GB sliding, GB migration, and grain rotation [24]. Although
173 the Coble creep formula (Eq. (5)) implies that grain growth reduces the creep rate, exper-
174 imental evidence suggests that the strain rate can also increase during deformation due to
175 GB migration, which acts as a stress-relaxation mechanism [24]. To suppress grain growth,
176 an idealized nanocrystalline microstructure of uniform grain sizes and shapes is usually used
177 in MD creep simulations [20, 21]. The geometry of grains can be closely modeled by the
178 space-filling 14-sided polyhedron known as the truncated octahedron [21, 37]. Truncated-
179 octahedral grains are nearly spherical, yet they display realistic grain features like triple
180 lines and quadruple junctions. Atomsk [31] was used to generate 16 truncated-octahedral
181 grains with random misorientations, and average grain diameters of 14, 16, 18, and 20 nm.
182 Based on our tests, smaller grain sizes (10 and 12 nm) suffered inconsistent evolution in creep
183 simulations at the highest temperature (i.e., 2000 K) and the lowest stress (i.e., 200 MPa).
184 Random grain misorientations lead to a relatively small fraction of low-angle GBs [21, 24];
185 thus, all GBs within a polycrystal can be considered high-angle GBs. Atoms with distances
186 smaller than $0.45a$, where a is the lattice parameter, were deleted to prevent unrealistically
187 high forces as an artifact of the structure generation process.

188 Based on initial tests, we found that the Kocevski potential stabilizes voids along GBs
189 in both bicrystals and polycrystals. This is likely due to the U-U repulsion in the Kocevski
190 potential and its inability to simulate metallic U [28]. Thus, the Kocevski potential cannot
191 be used for the study of Coble creep phenomena. Additionally, governed by the migration
192 of vacancies and atoms along GBs, accurate modeling of Coble creep requires reliable pre-
193 dictions of the energetics of vacancies and interstitials. The Tseplyaev potential provides
194 accurate formation and migration energies for both stoichiometric and non-stoichiometric
195 point defects that closely agree with DFT values [26, 28, 38]. On the other hand, the Ko-
196 cevski potential fails to reproduce accurate formation energies for U-rich and stoichiometric
197 conditions [28]. For these reasons, only the Tseplyaev potential is used to simulate the creep
198 behavior of UN.

199 Supercells are equilibrated in the *NPT* ensemble using the Nosé-Hoover thermostat and
200 barostat at temperatures of 1700–2000 K and zero pressure for 200 ps. Then, tensile stresses
201 in the range of 200–500 MPa are applied to the supercells in the *x*-direction for 5 ns. The
202 calculations were repeated using three different initial velocity distributions.

203 Diffusional creep is typically observed for $T > 0.5T_m$, where T_m is the melting point [18].
 204 For UN, the experimental melting temperature is about 3035 K at a nitrogen vapor pressure
 205 of 1 atm [39], and the Tsepelyaev potential predicts thermodynamic melting of UN at about
 206 2700 K [28]. Thus, diffusional creep is expected to be observed at the studied temperature
 207 range of 1700–2000 K. On the other hand, the applied stresses (i.e., 200–500 MPa) are an
 208 order of magnitude higher than typical experimental stresses at which creep is observed and
 209 will lead to strain rates in the range of 10^6 s^{-1} , which is several orders of magnitude higher
 210 than experimental creep rate values. However, such high stresses are required for creep to be
 211 observed within MD time scales. If we decrease the applied stress by an order of magnitude
 212 and increase the grain size from 10 nm to 10 μm , the strain rate becomes 10^{-4} – 10^{-5} s^{-1} —
 213 a typical experimental creep rate value. However, this would increase the computational
 214 cost to achieve a similar creep strain by approximately 10^4 times. It is expected that the
 215 fundamental physics of Coble creep is captured, given the computational setup applied here,
 216 and thus the extrapolation of conclusions from high stress/small grain simulations to more
 217 realistic stresses and grain sizes is considered reasonable. Ultrahigh strain rates have been
 218 traditionally used in MD modeling of Coble creep and tensile testing [20–22, 24, 29].

219 To visualize the microstructural details of the supercells, the centrosymmetry parameter
 220 (CSP) and the dislocation extraction algorithm (DXA) are utilized. The CSP has been
 221 calculated by OVITO for snapshots of the simulated supercells using the minimum-weight
 222 matching algorithm [40]. The CSP quantifies lattice disorder and is defined as [41]:

$$\text{CSP} = \sum_{i=1}^{N/2} |\mathbf{r}_i + \mathbf{r}_{i+N/2}|^2, \quad (6)$$

223 where N represents the number of nearest neighbors around an atom (for NaCl, $N = 6$), and
 224 \mathbf{r}_i and $\mathbf{r}_{i+N/2}$ are vectors extending from the atom in question to a pair of opposite neighbor-
 225 ing atoms. In a perfectly centrosymmetric crystal, contributions from all neighboring pairs
 226 cancel each other, yielding a CSP of zero. The CSP method is resilient to thermal noise;
 227 for a pristine crystal, it produces a single peak starting at zero, with its width broadening
 228 as temperature T increases. A second peak in the CSP graph indicates a different local
 229 structure, such as dislocations or highly disordered grain boundaries (GBs) [40, 42]. The
 230 CSP has units of squared distance, typically expressed as a^2 , where a is the lattice constant.
 231 The CSP serves as an indirect analysis method. For direct visualization of dislocations,
 232 OVITO’s DXA [43] is used, particularly applied to the U sub-lattice. A drawback of the
 233 DXA is its limitation in identifying predefined dislocations in single-component crystals, so
 234 dislocations with a Burgers vector outside the predefined families go undetected. This limits
 235 the algorithm’s ability to identify GB dislocations, which typically have much shorter Burg-
 236 ers vectors than those in the lattice [44]. Given that each sub-lattice in the B1 structure of
 237 UN forms a face-centered cubic (FCC) lattice, applying DXA to the U sub-lattice allows for
 238 precise dislocation identification and visualization.

239 3. Results

240 3.1. Direct simulation of Coble creep

241 A model microstructure of UN whose energy has been minimized at 0 K with a relative
 242 energy tolerance of 10^{-9} is shown in Fig. 1. The numbers of atoms in the constructed

polycrystals range between 1,547,344 atoms for the 14-nm polycrystal and 4,537,943 atoms for the 20-nm polycrystal, and the N/U ratio varies between 0.9999 and 1.0002. Each system is therefore either slightly hypo-stoichiometric or slightly hyper-stoichiometric, and any effect that may arise due to this slight off-stoichiometry is minor. Each creep rate is an average over three simulations using three different initial velocity distributions. To visualize the GB structure, atoms have been colored according to their CSP; yellow atoms have high CSP (i.e., high degree of miscoordination) and dark purple atoms have low CSP (i.e., low degree of miscoordination). Conceptually, low-angle GBs consist of isolated dislocation cores of high miscoordination that are separated by a nearly perfect crystal region of low miscoordination [45]. On the other hand, high-angle GBs consist of overlapping dislocation cores and display a high degree of miscoordination that is uniformly distributed along the GB area [24]. Hence, it can be concluded from the figure that virtually all of the GBs in the supercell are high-angle GBs which are visualized as continuous uninterrupted yellow lines. This also applies to all the supercells employed in this work. Networks of GB dislocations have also been observed along the GBs using the DXA in OVITO. These GB dislocations are not preferentially aligned with any slip plane, are essentially immobile, and do not give rise to any dislocation-dominated deformation that would interfere with diffusional creep. Additionally, sustainable plastic deformation via the dislocation–nucleation mechanism is not possible because, e.g., the stress required to activate a Frank–Read source (a principal mechanism to sustain plastic deformation via dislocation multiplication [46]) increases inversely with decreasing grain size ($\sigma \sim 1/d$), and the size of a Frank–Read source cannot exceed the grain size [21, 47]. Thus, our nanometer-sized grains are too small to accommodate a Frank–Read source that can be activated by typical stresses. It has also been visually confirmed that the microstructure does not undergo any micro-cracking, grain growth, GB sliding, or dislocation activity within grain interiors during the time scale of the simulation.

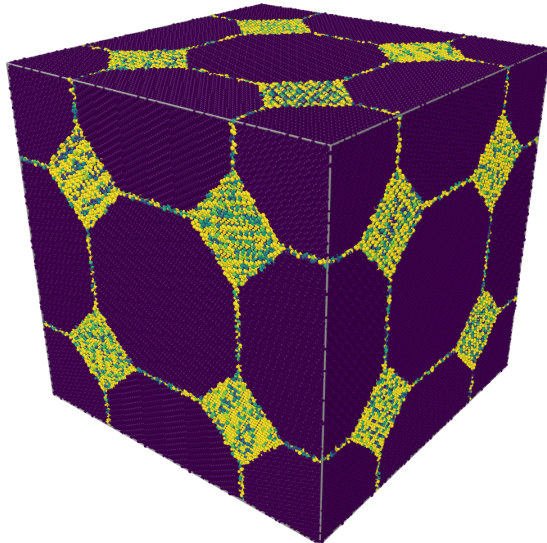


Figure 1: (Color online) UN polycrystalline supercell after energy minimization has been minimized at 0 K with a relative energy tolerance of 10^{-9} . To visualize the GB structure, atoms have been colored in OVITO according to their centrosymmetry parameter (CSP), where dark purple atoms have low CSP and yellow atoms have high CSP. For better visibility, the maximum CSP has been set to 20 \AA^2 .

268 Plots from the Coble creep simulations are shown in Fig. 2. An example of the strain
 269 variation with time is shown in Fig. 2a. After the instantaneous elastic strain, a transient
 270 strain stage is observed in which the strain rate decreases with time until it attains its
 271 steady-state value. Temperatures and stresses were chosen to maintain steady-state creep
 272 throughout the simulation while simultaneously ensuring a sufficient signal-to-noise ratio in
 273 the strain response. The strain rate is calculated using a linear fit to the final 3 ns of the strain
 274 versus time curve where steady-state creep is reached. The data was analyzed to parameterize
 275 Eq. (4). To calculate the activation energy of creep, the Arrhenius plots of the strain rate
 276 versus inverse temperature (e.g., Fig. 2b) have been fitted and an average value over all
 277 grain sizes and stresses calculated. As shown in Table 1, the calculated activation energy is
 278 $Q = 1.79 \pm 0.33$ eV, which is smaller than the activation energy of the Hayes correlation for
 279 thermal creep in UN (Eq. (1), $Q = 3.39$ eV [5]), which assumes a dislocation mechanism,
 280 and closer to the activation energy for GB diffusion in UN assumed by Konovalov *et al.*
 281 (i.e., $Q = 2.65$ eV) [12]. This indicates that Coble creep can be a competitive mechanism
 282 to dislocation creep in UN. It should be noted, however, that the large uncertainty in the
 283 activation energy can lead to more than an order of magnitude uncertainty in the predicted
 284 creep rate.

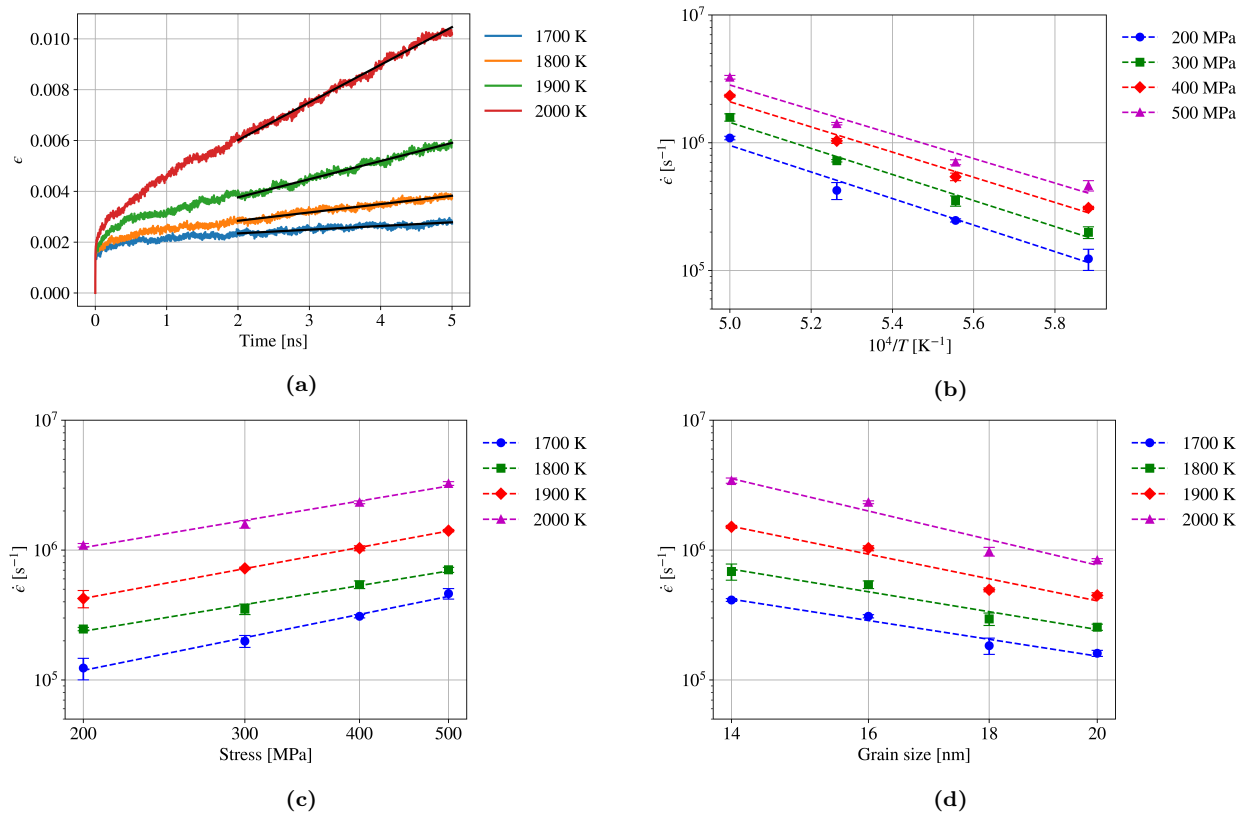


Figure 2: (Color online) (a) Variation of creep strain with time for a supercell with a grain size of 14 nm under constant stress of 200 MPa. (b) Semi-log plot of the variation of creep rate with inverse temperature for a supercell with a grain size of 16 nm. (c) Log-log plot of the variation of creep rate with stress for a supercell with a grain size of 16 nm. (d) Log-log plot of the variation of creep rate with grain size for supercells under constant stress of 400 MPa. In all figures, solid black lines correspond to the curve fits, and error bars correspond to one standard deviation.

Table 1: Coble creep parameters estimated from fitting the simulation results of the diffusional creep of UN. Uncertainties represent one standard deviation.

Activation energy, Q [eV]	Stress exponent, n	Grain size exponent, q
1.79 ± 0.33	1.35 ± 0.22	3.58 ± 0.87

To determine the dependence of the creep strain rate on the applied stress for each grain size and temperature, log-log plots of strain rate versus stress (Fig. 2c) have been fitted and the averaged value is shown in Table 1. A strain exponent $n = 1.35 \pm 0.22$ indicates that the stress dependence is nearly linear, which is characteristic of diffusional creep, and which agrees with the stress exponent found by Rogozkin *et al.* [9]. Following the same procedure for the stress exponent, the grain size exponent has been determined (Fig. 2d) for each applied stress and temperature, and the final averaged value is also shown in Table 1. It can be seen that the average grain size exponent $q = 3.58 \pm 0.87$ is very close to the grain size dependence of Coble creep ($q = 3$), but with relatively high uncertainty ($\sim 24\%$). Uncertainties of the fitting parameters in Table 1 are estimated by dividing the standard deviations by the mean values. It should be emphasized that only a subset of the data is shown in Figure 2, but the entire data set for all stresses, temperatures, and grain size are utilized in the determination of the average values in Table 1.

To confirm that the deformation mechanism is homogeneous (i.e., the total deformation of the supercell is proportional to the deformation of the individual grains), we visually confirmed that the positions of the centers of mass of the grains, normalized by the instantaneous lengths of the cubic simulation box, did not move during the time scale of the simulation. Additionally, using the “displacement vectors” modifier in OVITO [32] it was confirmed that only atoms along the GBs undergo motion during the time scale of the simulations. That is, only Coble creep is observed in our simulations and Nabarro-Herring creep is essentially absent at the considered temperatures and time scale.

3.2. Parameter-based Coble creep model

Following the methodology of Cooper *et al.* [25] for U_3Si_2 and Galvin *et al.* [23] for UO_2 , we also construct a parameter-based Coble creep model. In this approach, the parameters of the Coble creep formula (Eq. (5)) are calculated independently.

3.2.1. GB diffusivity

In ionic compounds like UN, the diffusional process requires ambipolar coupling to avoid compound decomposition [48]. This means that U and N atoms must diffuse in stoichiometric ratios with an effective diffusivity that is limited by the diffusivity of the slower species, i.e., uranium, along its fastest path. The total effective diffusivity is calculated based on Gordon’s formula [48] for ambipolar diffusion in an ionic solid $\text{A}_\alpha\text{B}_\beta$ (For UN, $\alpha = \beta = 1$):

$$D_{\text{eff}} = \frac{(\alpha + \beta)D_{\text{A}}D_{\text{B}}}{\beta D_{\text{A}} + \alpha D_{\text{B}}} \quad (7)$$

Eq. (7) differs from the usual formula for effective D by including the extra term $(\alpha + \beta)$, which appears because Gordon’s formulation is based on the molecular volume of $\text{A}_\alpha\text{B}_\beta$ whereas the traditional Coble creep formula (Eq. (5)) includes the average atomic volume

[22, 49]. Because we are dealing with polycrystals, it is difficult to exclusively track the atomic movement within the GBs to determine the GB diffusivity. Instead, we track the movement of all atoms within the polycrystals. In this picture, the total diffusivity of either U or N atoms has both bulk and GB components. According to the Hart formulation [50, 51], the total diffusivity in a polycrystal can be divided between bulk and GB components according to:

$$D = cD_{\text{GB}} + (1 - c)D_b, \quad (8)$$

where c is the fraction of atoms that belong to the GBs (c will be defined quantitatively later in Section 3.2.2), D_{GB} is the GB diffusivity, and D_b is the bulk diffusivity. Thus, with the knowledge of the total diffusivity in the polycrystals and the bulk diffusivity, the GB diffusivity can be readily estimated.

To calculate the bulk diffusivities of U and N atoms, an unbound Schottky pair is randomly introduced within a $50 \times 50 \times 50$ UN supercell which is then equilibrated at temperatures of 1700–2000 K and zero pressure under the *NPT* ensemble for 100 ps [52]. After equilibration, the mean squared displacements (MSD) of both species are averaged every 1 ps for a total simulation time of 5 ns. The results are shown in Fig. 3a. It is apparent that the U atoms do not diffuse within bulk UN and only undergo vibrational motion in their positions. N atoms start to show non-zero diffusivity only at 2000 K and only vibrate around their equilibrium positions at lower temperatures. According to the Einstein relation, $\text{MSD} = 6Dt$ in the limit of an infinite time. Fitting the MSD curve for N atoms at 2000 K over the final 3 ns gives $D_b^N = 5.91 \times 10^{-11} \text{ cm}^2/\text{s}$. This diffusivity value is negligible compared to the GB diffusivities of either U or N atoms (Fig. 3b, which will be described later in this subsection). Because U atoms do not undergo any measurable diffusivity, we can conclude that bulk diffusivity is essentially non-existent and all the atomic movement in the polycrystals can be solely attributed to GB diffusion.

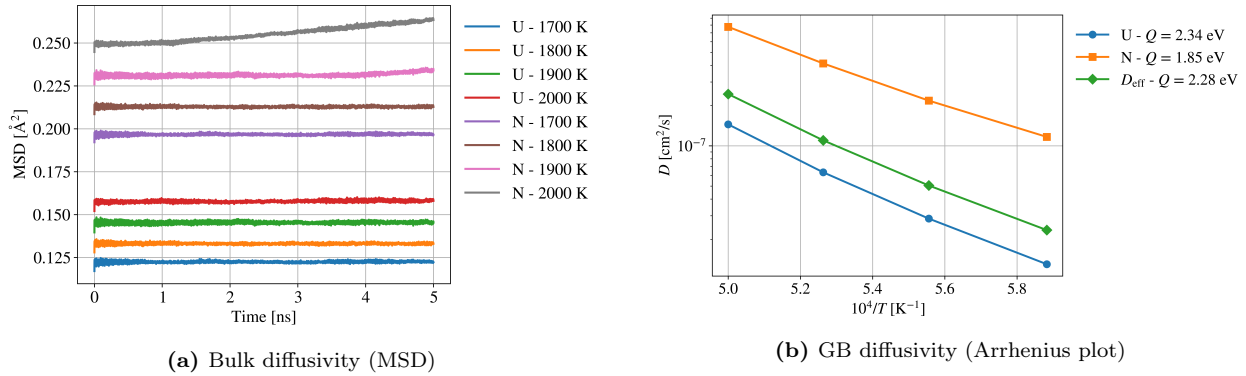


Figure 3: (Color online) (a) Mean squared displacements (MSD) of U and N atoms within bulk UN at different temperatures. A fit of the MSD curve for N atoms at 2000 K over the final 3 ns gives $D = 5.91 \times 10^{-11} \text{ cm}^2/\text{s}$. (b) Arrhenius plot of the GB diffusivity of U and N atoms, as well as the effective GB diffusivity. Note that the standard deviation of Q_U is $\pm 0.03 \text{ eV}$, and that of Q_N is $\pm 0.02 \text{ eV}$.

The motion of all atoms in stress-free polycrystals with a grain size of 20 nm has been tracked. The polycrystal is equilibrated at the target temperature and zero pressure within the *NPT* ensemble for 50 ps. Then, the MSD of all atoms of both types is averaged every 1 ps for a total averaging time of 5 ns. It was shown earlier that bulk diffusion is absent and

347 all the atomic movement is attributed to diffusion along the GBs. Diffusion in the direction
 348 perpendicular to a GB is usually much smaller than the other two directions spanned by
 349 the GB, and GB diffusion is treated as a two-dimensional (2D) phenomenon [51]. Thus, we
 350 calculate the GB diffusivity of each atomic species by a linear fit of the MSD of that species
 351 over the last 3 ns to the 2D Einstein relation:

$$D_{\text{GB}}^{\text{U,N}} = \frac{1}{c} \frac{\text{MSD}^{\text{U,N}}}{4t}. \quad (9)$$

352 The results of such calculations are shown in Fig. 3b. The calculation of the variable c
 353 for each temperature and grain size will be shown later. After getting the GB diffusivities of
 354 U and N atoms, the effective diffusivity is calculated based on Gordon's formula (Eq. (7)).
 355 The effective activation energy of GB diffusion is $Q = 2.28 \pm 0.09$ eV and the prefactor is
 356 $D_0 = 0.130 \pm 0.075$ cm²/s (which has the typical order of magnitude). It can be seen that
 357 the activation energy of GB diffusion in stress-free polycrystals ($Q_{\text{eff}} = 2.28$ eV) is closer
 358 to the assumed activation energy of GB diffusion in UN ($Q_{\text{GB}} = 2.65$ eV [12]) than the
 359 fitted activation energy of Coble creep simulation ($Q = 1.79$ eV). Additionally, we repeated
 360 the GB diffusion calculation for grains with sizes of 14–18 nm and found that the standard
 361 deviation of Q_{U} is ± 0.03 eV, and that of Q_{N} is ± 0.02 eV. Compared to this, the fitted
 362 activation energy of Coble creep has a larger uncertainty of ± 0.33 eV. This discrepancy can
 363 be attributed to the stress effect on GB diffusion. In general, GB diffusivity increases with
 364 the applied stress [24], which might be manifested by a reduction in the activation energy.
 365 A reduction in the activation energy stems from an increase of the GB diffusivity at the
 366 higher temperatures for which the stress effect on the GB diffusivity is more pronounced. It
 367 is also observed that the activation energy for the effective diffusivity is nearly dominated by
 368 that of U atoms, which confirms the assertion that the GB diffusion of the slowest-moving
 369 species, i.e., U atoms, is rate-limiting for Coble creep.

370 3.2.2. Grain-boundary width

371 Next, we closely analyze the GB width. At first, we need to differentiate between two
 372 concepts of GB width in high-purity materials [45, 53]: (a) diffusional GB width, δ_d , which
 373 corresponds to the width within which atoms diffuse, and (b) structural GB width, δ_s , which
 374 corresponds to the width within which miscoordinated atoms exist, whether they diffuse or
 375 not. Kebinski *et al.* [45] found in their atomistic simulations that δ_d is thermally activated
 376 and shows an Arrhenius dependence on temperature. However, their analysis was based on
 377 bicrystals, which usually contain symmetric tilt GBs and are not necessarily representative
 378 of realistic microstructures. Additionally, the analysis was conducted at temperatures near
 379 the melting point, which are not usually accessible in GB diffusion experiments due to the
 380 simultaneous contribution of bulk diffusion at these high temperatures. Thus, their results
 381 could not be experimentally verified. On the other hand, Prokoshkina *et al.* [53] conducted
 382 an extensive analysis of the measured GB widths of various metals and compounds and found
 383 that the GB widths measured in GB diffusion measurements do not show any dependence
 384 on temperature or grain size. The purpose of this section is to resolve this apparent conflict
 385 between atomistic simulations and experiments and provide a consistent definition for GB
 386 width that can be extracted from atomistic simulations and agrees with the experimental
 387 data. We begin by using our GB diffusivity data to extend the analysis from Kebinski *et al.*

³⁸⁸ to polycrystals of uniform size and shape and temperatures relatively far from the melting
³⁸⁹ point.

³⁹⁰ The diffusion flux at the GB (in m³/s) is a product of the GB diffusivity and diffusional
³⁹¹ GB width: $D_{\text{GB}}\delta_d$, and can be expressed as follows:

$$D_{\text{GB}}\delta_d = \lim_{t \rightarrow \infty} \frac{\Omega}{A} \frac{\sum_{i=1}^{N_{\text{GB}}} |\Delta \mathbf{r}_i(t)|^2}{6t} \approx \lim_{t \rightarrow \infty} \frac{\text{MSD}_{\text{GB}}(T)}{6t} \frac{\Omega N_{\text{GB}}(T)}{A} \quad (10)$$

³⁹² where both the MSD of GB atoms, MSD_{GB} , and the number of atoms *diffusing* within the
³⁹³ GB, N_{GB} , are functions of temperature. In [Appendix A](#), we derive the following formula
³⁹⁴ for the diffusional GB width of polycrystals:

$$\delta_d = \eta c V^{1/3} \quad (11)$$

³⁹⁵ where V is the volume of a space-filling grain and c is defined as the fraction of atoms that
³⁹⁶ have undergone non-affine displacements of at least the nearest-neighbor distance in the
³⁹⁷ limit of infinite simulation time. For UN, the nearest-neighbor distance is $0.5a$, where a is
³⁹⁸ the lattice parameter. c can be estimated using the displacement-vectors (DV) modifier in
³⁹⁹ OVITO [32] applied to snapshots of the polycrystal. η is a shape factor that depends on the
⁴⁰⁰ grain shape. For truncated-octahedral grains, $\eta = 0.376$ ([Eq. \(A.5\)](#)). Note that, unlike the
⁴⁰¹ calculation of the GB diffusivity which is based on averages taken during the MD simulation,
⁴⁰² the estimation of the GB width is a post-processing step.

⁴⁰³ Although [Eq. \(11\)](#) is derived for grains of uniform size and shape, it is principally applica-
⁴⁰⁴ ble to grains of random sizes and shapes provided that the average *grain volume* is treated
⁴⁰⁵ as the volume of a truncated octahedral grain and the grain size distribution is relatively
⁴⁰⁶ narrow. In this case, [Eq. \(11\)](#) can be readily applied to estimate δ_d for any polycrystal
⁴⁰⁷ using $\eta = 0.376$. The advantage of this method is that it enables us to determine δ_d for a
⁴⁰⁸ microstructure that contains realistic grain features like triple lines and quadruple junctions.
⁴⁰⁹ In contrast to other methods based on bicrystal simulations, our proposed method simulta-
⁴¹⁰ neously samples many GBs with various misorientations and gives an effective value for δ_d
⁴¹¹ averaged over all of them.

⁴¹² This analysis is implicitly based on two assumptions. First, in the limit of a very long
⁴¹³ time, the number of GB atoms that have moved by at least the nearest-neighbor distance
⁴¹⁴ will saturate to a value determined by the temperature. This was assumed by Keblinski *et*
⁴¹⁵ *al.* [45] but never proved. To demonstrate that this is indeed the case, we use OVITO's DV
⁴¹⁶ modifier to track the number of diffusing atoms in a stress-free 20-nm supercell. To probe
⁴¹⁷ the effect of the stress and the grain size on the diffusional GB width, we conduct the same
⁴¹⁸ analysis for the 20-nm supercell under stresses of 400 MPa and 500 MPa and the 18-nm
⁴¹⁹ supercell under a stress of 500 MPa. In all cases, the number of diffusing atoms is fitted to
⁴²⁰ a saturation function of the form:

$$N_{\text{GB}} = N_0 (1 - e^{-\lambda t}) + C \quad (12)$$

⁴²¹ In the limit of infinite time, the exponential approaches zero, and $N_{\text{GB}} = N_0 + C$. Note that
⁴²² N_{GB} represents the asymptotic (saturation) number of atoms participating in Coble creep
⁴²³ once steady-state grain boundary diffusion is fully established. The result of the fitting

for the 20-nm supercell under no stress is shown in Fig. 4a, which demonstrates that N_{GB} perfectly follows a saturation function, and that the saturated value of N_{GB} increases with increasing temperature. Similar trends have been observed for the other tracked supercells. The saturated values of $N_{\text{GB}} = N_0 + C$ are then fitted to an Arrhenius-type function. The results of such fitting for the tracked supercells are shown in Fig. 4b, which shows that the diffusional GB width perfectly follows an Arrhenius behavior that is independent of supercell grain size and applied stress. The activation energy for all tracked supercells is 0.74 ± 0.01 eV for the 20-nm supercell at all stress values and 0.82 eV for the 18-nm supercell. While the effect of grain size on Q_δ is quite small, the effect of stress is essentially non-existent. Based on their bicrystal calculation, Keblinski *et al.* [45] estimated the activation energy of the GB width in Pd to be 0.22 eV.

While these results corroborate the computational findings of Keblinski *et al.*, this Arrhenius dependence still contradicts the experimental observations that the measured GB width is independent of temperature. This leads to our second assumption: the GB width in the Coble creep formula corresponds to a temperature-independent (effective) GB width, which is calculated by extrapolating the diffusional GB width to the melting point where all miscoordinated atoms are assumed to have undergone diffusion. Extrapolating the Arrhenius curves in Fig. 4b to 2700 K (the melting point as predicted by the Tseplyaev potential [28]), the effective GB width is found to be $\delta = 2.69 \pm 0.08$ nm. This GB width should correspond to the diffusion of all the GB atoms and is the one we use in the parameter-based Coble creep formulation. We show later that this value of the GB width provides an excellent prediction of the prefactor in the phenomenological Coble creep formula, which supports our second assumption.

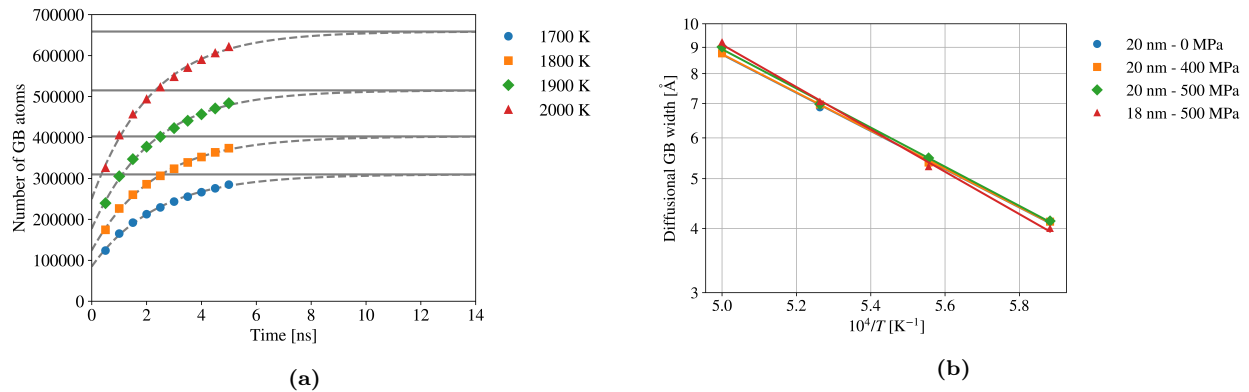


Figure 4: (Color online) (a) The variation of the number of GB atoms, N_{GB} , with time for the polycrystal with a grain size of 20 nm under no stress. In the limit of infinite time, N_{GB} reaches a saturation value that increases with increasing temperature. (b) Arrhenius plot of the diffusional GB width for the tracked supercells. The activation energy of δ_d ranged between 0.74 and 0.82 eV.

Lastly, we need to discuss the c parameter in Eq. (11), which is used in Eq. (9) to estimate the GB diffusivity. In analogy with the two definitions of the GB width, there are two definitions of the c parameter: (a) the fraction of atoms that diffuse within the GBs, and (b) the fraction of miscoordinated atoms existing within the GBs, whether they diffuse or not. A third definition [12] is to estimate c as the volume fraction of the GBs based on

452 the formula:

$$c = \frac{3\delta}{d} \quad (13)$$

453 where δ is the GB width, and d is the grain diameter. The same procedure of calculating
454 the GB width is used to extract the c parameter of the 20-nm polycrystal to calculate the
455 GB diffusivity in [Section 3.2.1](#). Note that the *saturated* number of GB atoms is linearly
456 proportional to the diffusional GB width ([Eq. \(A.1\)](#)), and, thus, both follow an Arrhenius
457 behavior with the same activation energy. Like the GB width, we extrapolate the Arrhenius
458 plot of the saturated number of GB atoms up to the melting temperature to extract the
459 number of miscoordinated atoms. This number is then divided by the total number of atoms
460 in the supercell to get c . Based on this procedure, $c = 0.44 \pm 0.01$ for the stress-free 20-nm
461 polycrystal. It should be noted that if we used $\delta = 2.69$ nm, and $d = 20$ nm in [Eq. \(13\)](#),
462 we get $c = 0.40$. That is, the definitions of c based on the volume fraction or the atomic
463 fraction give very close results and can be used interchangeably. For macroscopic systems
464 with d in the μm -range, $c \sim 10^{-3}$. In effect, c penalizes the nm-sized structures for having
465 grains with a large surface-to-volume ratio.

466 *3.2.3. Vacancy volume*

467 The remaining unknown parameter in the Coble creep model ([Eq. \(5\)](#)) is the vacancy
468 volume. To calculate the vacancy volume in UN, we construct $6 \times 6 \times 6$ perfect supercells
469 and calculate the volume of the minimized structure at 0 K. Then, we separately delete U
470 and N atoms from the center of the supercell, minimize the energy of the defective structure,
471 and finally calculate the vacancy volume as the volume difference between the pristine and
472 defective crystals. All structures have been minimized with a relative energy tolerance of
473 10^{-9} . The result of such calculations is presented in [Table 2](#), where the atomic volume is also
474 given for reference. We use the values of the Tsepelyaev potential, but those calculated by
475 the Kocevski potential are also shown for comparison. It can be observed that the Kocevski
476 potential predicts a positive volume for the N vacancy, which is unphysical. The reason for
477 this is that upon removing the N atom, there is no longer a screening/shielding between the
478 U atoms, which repel each other and lead to an increase in the volume of the supercell with
479 the vacancy. This is due to the inability of the Kocevski potential to model metallic U. From
480 [Table 2](#), we take the absolute value of V_U as the vacancy volume, i.e., $\Omega = 4.963 \text{ \AA}^3$. The
481 vacancy volume is nearly one-third of the atomic volume (13.909 \AA^3), indicating that the
482 commonly used approximation of equating Ω to atomic volume [[18](#)] is not accurate for UN.
483 The discrepancy arises from the local lattice relaxation and volume shrinkage induced by the
484 formation of a vacancy, highlighting the importance of calculating Ω explicitly. To conclude,
485 all the values for the parameter-based Coble creep model are summarized in [Table 3](#).

Table 2: Vacancy and atomic volumes (in \AA^3) as predicted by the Tsepelyaev and Kocevski potentials. $\Omega(\text{atom})$ is the average volume of a single atom.

	$\Omega(V_U)$	$\Omega(V_N)$	$\Omega(\text{atom})$
Tsepelyaev potential	-4.963	-0.227	13.909
Kocevski potential	-1.990	4.350	14.685

486 As a sanity check of our calculated parameters, according to the Mukherjee-Bird-Dorn
487 phenomenological model of Coble creep [[33](#)], the product $A_C \Omega \delta$ should numerically equal

488 $50b^4$ where b is the Burgers vector. With $A_C = 46.347$, we find that $A_C\Omega\delta = 6195 \text{ \AA}^4$,
 489 whereas $50b^4 = 6691 \text{ \AA}^4$, with a difference of only 7.52%. This also supports our method
 490 in calculating the GB width and its associated assumptions. In other words, although
 491 atomistic simulations reveal a temperature-dependent diffusional GB width, this behavior
 492 is not attributed to the limited timescales accessible to MD. Rather, our analysis shows
 493 that the number of diffusing atoms within GBs saturates with time and increases with
 494 temperature, resulting in an Arrhenius dependence of the diffusional GB width. In contrast,
 495 experimental GB widths reflect a long-time effective value that is typically temperature-
 496 independent. Additionally, the experimentally measured GB width can vary depending on
 497 the measurement technique. High-resolution transmission electron microscopy (HRTEM)
 498 yields the structural GB width, which is precise but not directly relevant to diffusional creep
 499 studies [53]. In contrast, GB widths inferred from diffusion data are more relevant but are
 500 less reliable due to uncertainties associated with data fitting [53]. To reconcile simulation
 501 and experimental perspectives, we extrapolated the temperature-dependent diffusional GB
 502 width to the melting point and defined this extrapolated value as the effective GB width to be
 503 used in the Coble creep formulation. This value (2.69 nm) reproduces the expected prefactor
 504 in the Coble creep equation and provides a consistent physical basis for incorporating MD-
 505 based GB width estimates into mesoscale models. It should be mentioned that the proposed
 506 method for estimating the effective GB width is general and transferable, as it relies solely
 507 on atomistic trajectories and makes no assumptions about the material's chemistry, crystal
 508 structure, or defect energetics.

Table 3: Values for the parameter-based Coble creep model.

Coble prefactor, A_C	46.347
Vacancy volume, Ω	$4.963 \times 10^{-30} \text{ m}^3$
Effective GB width, δ	$2.69 \times 10^{-9} \text{ m}$
GB diffusivity prefactor, D_0	$1.30 \times 10^{-5} \text{ m}^2/\text{s}$
GB diffusivity activation energy, Q	2.28 eV

509 3.2.4. Comparison of Creep Predictions

510 We compare the simulation and parameter-based models of Coble creep in UN developed
 511 in this work to Coble creep in UO_2 as calculated by Galvin *et al.* [23]. The prefactor in
 512 the simulation model was calculated by utilizing the values in [Table 1](#) within [Eq. \(4\)](#). The
 513 prefactor was found to have a numerical value of $A = 3.424 \times 10^{-26}$. For both fuels, a stress
 514 of 15 MPa, and a grain size of 10 μm were assumed. The result of such a comparison is
 515 shown in [Fig. 5](#). It can be seen that the two models of Coble creep in UN agree to less than
 516 an order of magnitude, especially at lower temperatures. Additionally, irrespective of the
 517 creep model, the Coble creep rate of UN is approximately one order of magnitude larger than
 518 that of UO_2 . It is also an order of magnitude larger than the Hayes *et al.* correlation for
 519 dislocation creep in UN. Although a stress of 15 MPa is outside the stress range of the Hayes
 520 creep correlation (i.e., 20–34 MPa), it is not very far from the range's lower limit, and we
 521 assume it can at least provide an estimate of the dislocation creep rate for stresses slightly
 522 smaller or larger than the reported stress applicability range. This comparison shows that
 523 Coble creep in UN can be more dominant than (or is at least competitive with) dislocation

524 creep. This agrees with the qualitative analysis by Konovalov *et al.* [12]. It should be
 525 mentioned that Galvin *et al.* [23] used a Coble creep prefactor $A_C = 42\pi$ for their UO_2
 526 Coble creep formula, whereas in this work, we use $A_C = 46.347$. However, the difference
 527 between the two values is only a factor of 3, which would have little effect on the results in
 528 Fig. 5.

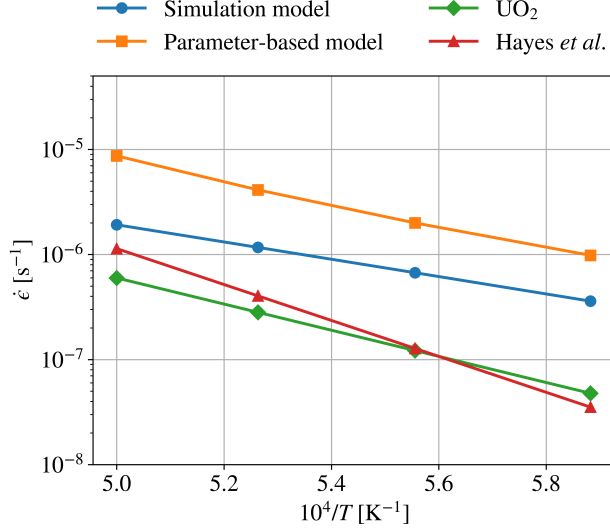


Figure 5: Comparison between the simulation and parameter-based models of Coble creep in UN developed in this work to Coble creep in UO_2 in the temperature range 1700–2000 K for a stress of 15 MPa, and a grain size of $10 \mu\text{m}$. The UO_2 data is taken from [23]. The Hayes *et al.* [5] correlation for dislocation creep is also presented for comparison.

529 Merely comparing the properties of different fuel systems within a temperature range
 530 might not accurately represent how the fuel systems behave in reactor conditions. More
 531 appropriately, we should compare fuel behaviors at representative center-line temperatures
 532 [54]. Considering the high thermal conductivity of UN, it is expected that the center-line
 533 temperatures and temperature gradients of UN fuel rods are much lower than those of UO_2
 534 fuel rods under the same conditions. For example, based on their finite-element analysis of
 535 the thermal-mechanical behavior of several advanced fuel-cladding combinations, Zeng *et al.*
 536 [55] have estimated the early-life centerline temperature of the $\text{UO}_2\text{-FeCrAl}$ fuel system to be
 537 about 1300 K, whereas it is only about 900 K for the UN-FeCrAl fuel system. Thus, under
 538 the same early-life reactor conditions, the creep of UN is expected to be less pronounced
 539 than that of UO_2 . The effect of irradiation on this comparison, however, requires a separate
 540 study.

541 4. Discussion

542 Parameters in Table 1 calculated from the fitting of the diffusional creep simulation have
 543 about 16-24% uncertainty, which is reasonable considering that each strain rate is an average
 544 over three unique simulations. The uncertainty can be reduced by simulating for longer times
 545 or averaging over more runs. However, this is computationally expensive for the supercells
 546 at hand, whose number of atoms ranges between 1,547,344 atoms for the 14-nm polycrystal

547 and 4,537,943 atoms for the 20-nm polycrystal. Due to the much lower computational cost
 548 and smaller uncertainties, the parameter-based Coble creep model is recommended for use
 549 in the determination of a Coble creep rate.

550 While the simulations presented in this work utilize nanometer-scale polycrystals (14–20
 551 nm) to achieve sufficient creep strain within accessible MD time scales, the fundamental
 552 deformation mechanism, namely, diffusional creep mediated by GB diffusion, is governed
 553 by well-established scaling laws. The Coble creep model inherently accounts for grain size
 554 effects, combined with the several hundred MPa stresses, through its σ/d^3 dependence,
 555 enabling extrapolation of MD-obtained parameters to realistic microstructural scales (on
 556 the order of micrometers) and typical creep stresses (tens of MPa).

557 An important aspect of this work is that we investigated the temperature dependence
 558 of the diffusional GB width and proposed a consistent method to calculate an effective GB
 559 width for the Coble creep formula. We found that the diffusional GB width in UN follows
 560 an Arrhenius behavior with an activation energy of about $Q_\delta = 0.74\text{--}0.82$ eV. Kebinski
 561 *et al.* [45] assumed that the activation energy of GB diffusion ($Q = 2.28$ eV in our case)
 562 can be expressed as $Q = Q_\delta + Q_{\text{amorph}}$, where Q_{amorph} is the activation energy for diffusion
 563 in the amorphous structure of the GB. Based on this assumption, Q_{amorph} should be 1.47–
 564 1.55 eV. For this assumption to be verified experimentally, amorphous diffusion coefficients
 565 need to be measured for UN. However, it was never reported that UN amorphizes under
 566 irradiation. However, this does not affect our estimated GB width which nearly perfectly
 567 predicts the prefactor of the Coble creep formula, i.e., Eq. (5). Our two Coble creep models
 568 closely agree, especially at lower temperatures. However, considering that the parameter-
 569 based model generally exhibits smaller uncertainties in its calculated parameters, is much
 570 less computationally expensive, and can be more easily extended to a larger temperature
 571 range, we recommend its use in fuel performance codes. For ease of access, the complete
 572 Coble creep rate equation is provided here:

$$\dot{\epsilon} = 582610.427 \frac{\sigma}{Td^3} \exp\left(-\frac{2.28 \text{ eV}}{k_B T}\right), \quad (14)$$

573 where σ is the stress in MPa, T is the temperature in K, d is the average grain size in μm ,
 574 and $\dot{\epsilon}$ is the creep rate in s^{-1} .

575 The activation energy of Coble creep in UN is about 1 eV smaller than that of the
 576 dislocation-mediated creep estimated by Hayes *et al.* [5] and is very close to the activation
 577 energy of GB diffusion in UN assumed by Konovalov *et al.* [12]. This implies that there is
 578 a surface in the σ, d, T -space that separates regions in which Coble creep is dominant from
 579 other regions where dislocation creep is dominant. To examine this idea in some detail, we use
 580 Eqs. (1) and (14) (our Coble creep correlation and the Hayes dislocation creep correlation)
 581 to construct deformation mechanism maps for UN to identify regions where Coble creep is
 582 dominant and others where dislocation creep is dominant. Deformation mechanism maps
 583 that examine the dominant creep mechanisms for different grain sizes and stresses at $T =$
 584 1800 K and 2200 K are shown in Figs. 6a and 6b, respectively. As expected, as the grain size
 585 is increased, dislocation creep becomes more dominant. The red solid line in Figs. 6a and 6b
 586 refers to the grain size and stress range of the creep rate measurements by Fassler *et al.* [6],
 587 which had a stress exponent of about 4.7. The measurements are clearly in the dislocation
 588 creep region which explains the high stress exponent. It should be mentioned that Fassler

589 *et al.* data were obtained at 1373–1623 K.

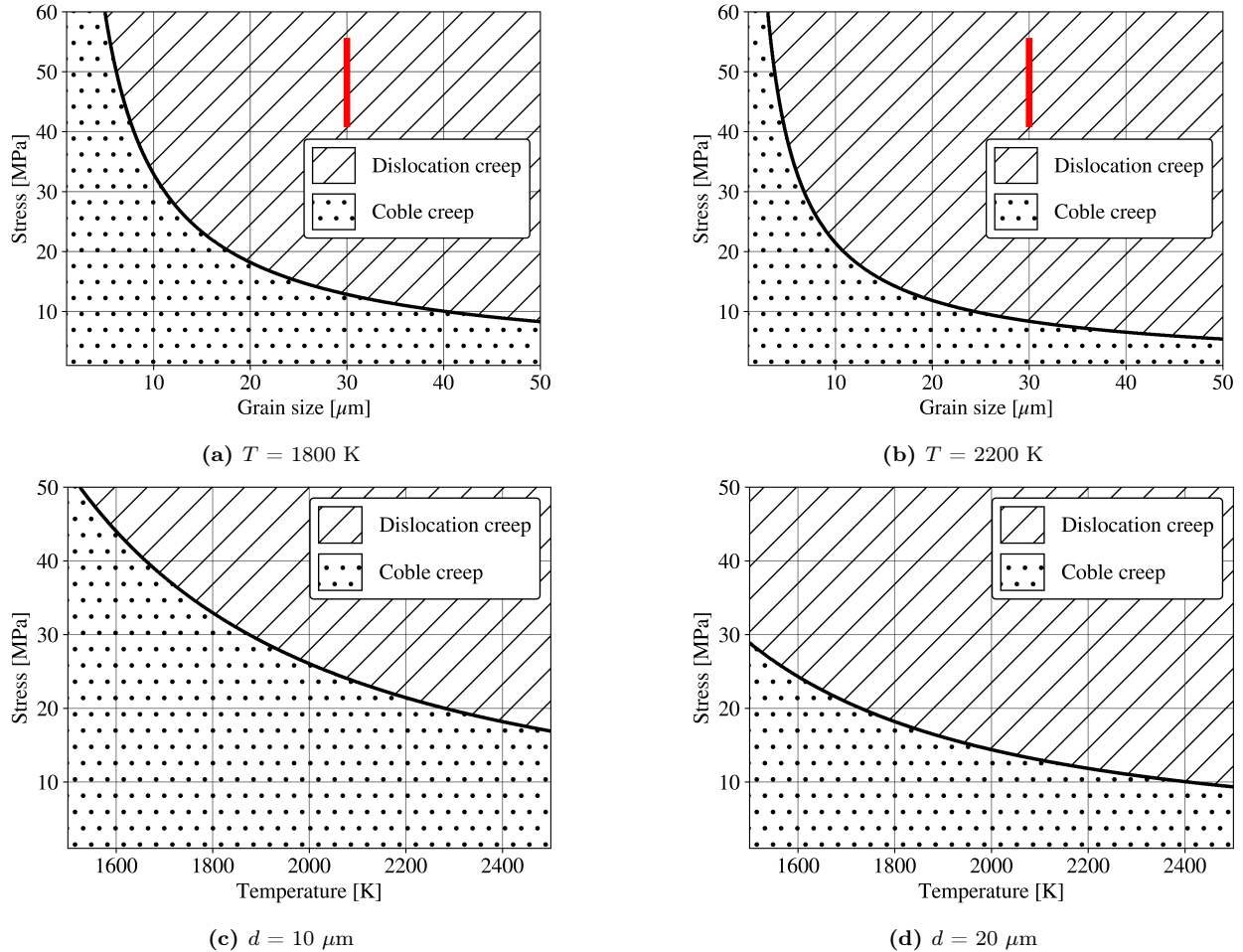


Figure 6: (Color online) Deformation mechanism maps of the dominant creep mechanism for different grain sizes and stresses at (a) $T = 1800 \text{ K}$ and (b) $T = 2200 \text{ K}$. The red solid line in (a) and (b) refers to the grain size and stress range of the creep rate measurements by Fassler *et al.* [6]. Deformation mechanism maps of the dominant creep mechanism for different temperatures and stresses at (c) $d = 10 \mu\text{m}$ and (d) $d = 20 \mu\text{m}$.

590 Interestingly, at $d = 10 \mu\text{m}$, the upper limit of the optimum UN grain sizes [14], and
 591 the stress range of 20–30 MPa, within which the Hayes correlation was fitted, Coble creep is
 592 more dominant than dislocation creep at 1800 K, and both are nearly equally present at 2200
 593 K. Thus, a contribution of both creep mechanisms will be observed with the contribution
 594 of the dislocation creep increasing with increasing temperature or increasing the grain size.
 595 Similar deformation mechanism maps for $d = 10$ and $20 \mu\text{m}$ are shown in Figs. 6c and 6d,
 596 respectively, for different temperatures and stresses. For a stress of 20 MPa and $d = 10$
 597 μm , dislocation creep becomes apparent at about $T = 2200 \text{ K}$, whereas for $d = 20 \mu\text{m}$,
 598 Coble creep is only present at temperatures below $T = 1700 \text{ K}$, where the creep rate is
 599 small anyway. The most general thermal creep correlation for UN should be a sum of both

600 contributions:

$$\dot{\epsilon}_{\text{tot}} = 582610.427 \frac{\sigma}{Td^3} \exp\left(-\frac{2.28 \text{ eV}}{k_B T}\right) + 2.054 \times 10^{-3} \sigma^{4.5} \exp\left(-\frac{3.39 \text{ eV}}{k_B T}\right), \quad (15)$$

601 where T is in K, σ is in MPa, and d is in μm . To test this final correlation, we compare it to
602 the experimental data of Uchida and Ichikawa [8] in Fig. 7. For the grain size of 9 μm , the
603 correlation gives an excellent prediction of the experimental creep rate. For the grain size
604 of 15 μm , Eq. (15) underestimates the creep rate by at most an order of magnitude, which
605 can be considered fair qualitative agreement taking into account that the 15- μm samples of
606 Uchida and Ichikawa [8] experienced a significant hot-pressing effect.

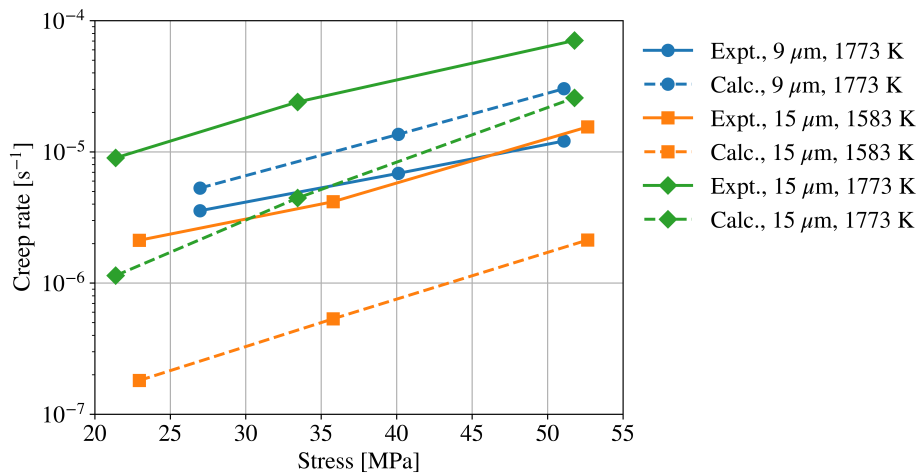


Figure 7: (Color online) Comparison of the experimental creep rate data of Uchida and Ichikawa [8] to that calculated using Eq. (15).

607 While the present work addresses thermally activated diffusional creep in pristine UN,
608 irradiation is expected to significantly influence creep behavior under reactor-relevant conditions.
609 In particular, irradiation-enhanced diffusion can markedly increase atomic transport
610 rates and enable creep rates far exceeding those predicted from thermal diffusion alone [25].
611 Consequently, the results presented here should be interpreted as a lower bound on in-service
612 creep behavior and motivate future studies that explicitly incorporate radiation damage.

613 5. Conclusions

614 In this study, we employed MD simulations to investigate specific aspects of the mechanical behavior of UN. The diffusional creep simulations were conducted using nanometer-sized
615 polycrystals with realistic microstructural features. Results indicate that Nabarro-Herring
616 creep is not active within the studied temperature range and time scale. Instead, Coble
617 creep emerges as the dominant diffusional creep mechanism, exhibiting an activation energy
618 of 2.28 eV. A method is introduced to compute the diffusional GB width and its tempera-
619 ture dependence in polycrystals. The diffusional GB width of UN is observed to follow an
620 Arrhenius behavior with an activation energy of 0.74–0.82 eV. The value of the diffusional
621 GB width at the melting point is estimated as 2.69 nm, which we treat as an effective GB
622 width.

width to be used in the Coble creep formula. This value shows an excellent prediction of the prefactor of the phenomenological Coble creep formula. The parameter-based model of Coble creep in UN agrees with the simulation model and shows less uncertainty at less computational cost. It is shown that the most general thermal creep correlation of UN is a sum of our Coble creep correlation and the Hayes *et al.* dislocation creep correlation.

6. Acknowledgements

The authors thank Khadija Mahbuba and Mahmoud Hawary for the fruitful discussions and useful suggestions. This work is funded by Westinghouse Electric Company. This research made use of the resources of the High-Performance Computing Center at Idaho National Laboratory, which is supported by the Office of Nuclear Energy of the U.S. Department of Energy and the Nuclear Science User Facilities under Contract No. DE-AC07-05ID14517. Mohamed AbdulHameed dedicates this work to Ayman AbdulRaheem.

Appendix A. Derivation of the diffusional GB width formula

An estimate of the diffusional GB width can be made based on the formula [45]:

$$\delta_d = \frac{N_{\text{GB}}\Omega}{A} \quad (\text{A.1})$$

where N_{GB} is the number of atoms existing within the GBs, Ω is the atomic volume, and A is the GB area. The number of GB atoms can be defined as $N_{\text{GB}} = cN$ [24] where c is defined as the fraction of atoms that have undergone non-affine displacements of at least one nearest-neighbor distance in the limit of infinite simulation time, and N is the total number of atoms in the supercell. The atomic volume is $\Omega = gV/N$, where g is the number of grains in the supercell (in our case, $g = 16$), and V is the grain volume. Because the grains are space-filling, the supercell volume $l_x l_y l_z = gV$. The GB area is $A = gS/2$, where S is the grain surface area, which for a truncated octahedron is given by [56]:

$$S = (6 + 12\sqrt{3}) l^2 \quad (\text{A.2})$$

where l is the truncated octahedron's edge length, which can be calculated from [56]:

$$l = \left(\frac{V}{8\sqrt{2}} \right)^{1/3} \quad (\text{A.3})$$

Thus, for the case of a supercell containing truncated-octahedral grains of uniform size and shape, the diffusional GB width is:

$$\delta_d = 2c \frac{V}{S} = \eta c V^{1/3} \quad (\text{A.4})$$

where η is a shape factor that depends on the grain shape. For truncated-octahedral grains:

$$\eta = \frac{4 \times 2^{1/3}}{3 + 6\sqrt{3}} \approx 0.376. \quad (\text{A.5})$$

649 This derivation assumes that the grains are space-filling and of uniform shape and size. It is
650 interesting to note in Eq. (A.4) that while the GB width, δ , depends on the grain volume-
651 to-surface ratio, V/S , which increases with increasing the grain size, δ also depends on c ,
652 which increases both with increasing the temperature and the grain surface-to-volume ratio.
653 That is, this definition of the GB width takes into account both structural and diffusional
654 aspects.

655 **References**

- 656 [1] C. Ekberg, D. R. Costa, M. Hedberg, M. Jolkonen, Nitride fuel for Gen IV nuclear
657 power systems, Journal of Radioanalytical and Nuclear Chemistry 318 (2018) 1713–
658 1725. [doi:10.1007/s10967-018-6316-0](https://doi.org/10.1007/s10967-018-6316-0).
- 659 [2] J. Wallenius, Nitride fuels, Comprehensive Nuclear Materials 5 (2020) 88–101. [doi:10.1016/B978-0-12-803581-8.11694-7](https://doi.org/10.1016/B978-0-12-803581-8.11694-7).
- 660 [3] M. Uno, T. Nishi, M. Takano, Thermodynamic and thermophysical properties of
661 the actinide nitrides, Comprehensive Nuclear Materials: Second Edition (2020) 202–
662 231[doi:10.1016/B978-0-12-803581-8.11749-7](https://doi.org/10.1016/B978-0-12-803581-8.11749-7).
- 663 [4] D. Frazer, B. Maiorov, U. Carvajal-Nuñez, J. Evans, E. Kardoulaki, J. Dunwoody, T. A.
664 Saleh, J. T. White, High temperature mechanical properties of fluorite crystal structured
665 materials (CeO_2 , ThO_2 , and UO_2) and advanced accident tolerant fuels (U_3Si_2 , UN, and
666 UB_2), Journal of Nuclear Materials 554 (2021). [doi:10.1016/j.jnucmat.2021.153035](https://doi.org/10.1016/j.jnucmat.2021.153035).
- 667 [5] S. L. Hayes, J. K. Thomas, K. L. Peddicord, Material property correlations for uranium
668 mononitride II. mechanical properties, Journal of Nuclear Materials 171 (1990) 271–288.
- 669 [6] M. Fassler, F. Huegel, M. DeCrescente, The compressive creep of UC and UN, Tech.
670 Rep. PWAC-482, Pratt & Whitney Aircraft Co. (1965).
- 671 [7] R. Vandervoort, W. Barmore, C. Cline, Compressive creep of polycrystalline uranium
672 mononitride in nitrogen, Transactions of the Metallurgical Society of AIME 242 (1968)
673 1466–1467.
- 674 [8] M. Uchida, M. Ichikawa, Compressive creep of sintered UC-UN solid solutions, Journal
675 of Nuclear Materials 49 (1973). [doi:10.1016/0022-3115\(73\)90065-2](https://doi.org/10.1016/0022-3115(73)90065-2).
- 676 [9] B. D. Rogozkin, N. M. Stepenova, A. A. Proshkin, Mononitride fuel for fast reactors,
677 Atomic Energy 95 (2003). [doi:10.1023/B:ATEN.0000007886.86817.32](https://doi.org/10.1023/B:ATEN.0000007886.86817.32).
- 678 [10] M. Meyers, K. Chawla, Mechanical Behavior of Materials, 2nd Edition, Cambridge
679 University Press, 2009.
- 680 [11] E. A. Kotomin, Y. A. Mastrikov, S. N. Rashkeev, P. V. Uffelen, Implementing first
681 principles calculations of defect migration in a fuel performance code for UN simulations,
682 Journal of Nuclear Materials 393 (2009) 292–299. [doi:10.1016/j.jnucmat.2009.06.016](https://doi.org/10.1016/j.jnucmat.2009.06.016).

- 685 [12] I. I. Konovalov, B. A. Tarasov, E. M. Glagovsky, Structural-phase state and creep of
686 mixed nitride fuel, in: IOP Conference Series: Materials Science and Engineering, Vol.
687 130, 2016. [doi:10.1088/1757-899X/130/1/012030](https://doi.org/10.1088/1757-899X/130/1/012030).
- 688 [13] J. Adachi, K. Kurosaki, M. Uno, S. Yamanaka, M. Takano, M. Akabori, K. Minato, Me-
689 chanical properties at sub-microscale and macroscale of polycrystalline uranium monon-
690 itride, Journal of Nuclear Materials 384 (2009) 6–11. [doi:10.1016/j.jnucmat.2008.09.019](https://doi.org/10.1016/j.jnucmat.2008.09.019).
- 692 [14] K. D. Johnson, D. A. Lopes, Grain growth in uranium nitride prepared by spark plasma
693 sintering, Journal of Nuclear Materials 503 (2018). [doi:10.1016/j.jnucmat.2018.02.041](https://doi.org/10.1016/j.jnucmat.2018.02.041).
- 695 [15] K. Yang, E. Kardoulaki, D. Zhao, A. Broussard, K. Metzger, J. T. White, M. R. Sivack,
696 K. J. McClellan, E. J. Lahoda, J. Lian, Uranium nitride (UN) pellets with controllable
697 microstructure and phase - fabrication by spark plasma sintering and their thermal-
698 mechanical and oxidation properties, Journal of Nuclear Materials 557 (2021). [doi:10.1016/j.jnucmat.2021.153272](https://doi.org/10.1016/j.jnucmat.2021.153272).
- 700 [16] L. He, M. Khafizov, C. Jiang, B. Tyburska-Püschel, B. J. Jaques, P. Xiu, P. Xu, M. K.
701 Meyer, K. Sridharan, D. P. Butt, J. Gan, Phase and defect evolution in uranium-
702 nitrogen-oxygen system under irradiation, Acta Materialia 208 (2021). [doi:10.1016/j.actamat.2021.116778](https://doi.org/10.1016/j.actamat.2021.116778).
- 704 [17] J. C. Mauro, Materials Kinetics: Transport and Rate Phenomena, 1st Edition, Elsevier,
705 2020.
- 706 [18] T. Courtney, Mechanical Behavior of Materials, 2nd Edition, Waveland Press, Inc.,
707 2005.
- 708 [19] S. L. Hayes, J. K. Thomas, K. L. Peddicord, Material property correlations for uranium
709 mononitride III. transport properties, Journal of Nuclear Materials 171 (1990) 289–299.
- 710 [20] P. Kebbinski, D. Wolf, H. Gleiter, Molecular-dynamics simulation of grain-boundary
711 diffusion creep, Interface Science 6 (1998). [doi:10.1023/A:1008664218857](https://doi.org/10.1023/A:1008664218857).
- 712 [21] V. Yamakov, D. Wolf, S. R. Phillpot, H. Gleiter, Grain-boundary diffusion creep in
713 nanocrystalline palladium by molecular-dynamics simulation, Acta Materialia 50 (2002).
714 [doi:10.1016/S1359-6454\(01\)00329-9](https://doi.org/10.1016/S1359-6454(01)00329-9).
- 715 [22] T. G. Desai, P. C. Millett, D. Wolf, Molecular dynamics study of diffusional creep in
716 nanocrystalline UO₂, Acta Materialia 56 (2008). [doi:10.1016/j.actamat.2008.02.052](https://doi.org/10.1016/j.actamat.2008.02.052).
- 718 [23] C. O. Galvin, D. A. Andersson, R. T. Sweet, L. Capolungo, M. W. Cooper, Diffusional
719 creep model in UO₂ informed by lower-length scale simulations, Journal of Nuclear Ma-
720 terials 607 (2025) 155659. [doi:https://doi.org/10.1016/j.jnucmat.2025.155659](https://doi.org/10.1016/j.jnucmat.2025.155659).

- [24] A. J. Haslam, V. Yamakov, D. Moldovan, D. Wolf, S. R. Phillpot, H. Gleiter, Effects of grain growth on grain-boundary diffusion creep by molecular-dynamics simulation, Acta Materialia 52 (2004). [doi:10.1016/j.actamat.2003.12.048](https://doi.org/10.1016/j.actamat.2003.12.048).
- [25] M. W. Cooper, K. A. Gamble, L. Capolungo, C. Matthews, D. A. Andersson, B. Beeler, C. R. Stanek, K. Metzger, Irradiation-enhanced diffusion and diffusion-limited creep in U₃Si₂, Journal of Nuclear Materials 555 (2021). [doi:10.1016/j.jnucmat.2021.153129](https://doi.org/10.1016/j.jnucmat.2021.153129).
- [26] V. I. Tseplyaev, S. V. Starikov, The atomistic simulation of pressure-induced phase transition in uranium mononitride, Journal of Nuclear Materials 480 (2016) 7–14. [doi:10.1016/j.jnucmat.2016.07.048](https://doi.org/10.1016/j.jnucmat.2016.07.048).
- [27] V. Kocevski, M. W. Cooper, A. J. Claisse, D. A. Andersson, Development and application of a uranium mononitride (UN) potential: Thermomechanical properties and Xe diffusion, Journal of Nuclear Materials 562 (2022). [doi:10.1016/j.jnucmat.2022.153553](https://doi.org/10.1016/j.jnucmat.2022.153553).
- [28] M. AbdulHameed, B. Beeler, C. O. Galvin, M. W. Cooper, Assessment of uranium nitride interatomic potentials, Journal of Nuclear Materials (2024) 155247 [doi:https://doi.org/10.1016/j.jnucmat.2024.155247](https://doi.org/10.1016/j.jnucmat.2024.155247).
- [29] M. AbdulHameed, B. Beeler, A. Claisse, Atomistic investigation of plastic deformation and dislocation motion in uranium mononitride, Applied Sciences 15 (2025) 2666. [doi:https://doi.org/10.3390/app15052666](https://doi.org/10.3390/app15052666).
- [30] A. P. Thompson, H. M. Aktulga, R. Berger, D. S. Bolintineanu, W. M. Brown, P. S. Crozier, P. J. in 't Veld, A. Kohlmeyer, S. G. Moore, T. D. Nguyen, R. Shan, M. J. Stevens, J. Tranchida, C. Trott, S. J. Plimpton, LAMMPS—a flexible simulation tool for particle-based materials modeling at the atomic, meso, and continuum scales, Computer Physics Communications 271 (2022). [doi:10.1016/j.cpc.2021.108171](https://doi.org/10.1016/j.cpc.2021.108171).
- [31] P. Hirel, Atomsk: A tool for manipulating and converting atomic data files, Computer Physics Communications 197 (2015). [doi:10.1016/j.cpc.2015.07.012](https://doi.org/10.1016/j.cpc.2015.07.012).
- [32] A. Stukowski, Visualization and analysis of atomistic simulation data with OVITO—the open visualization tool, Modelling and Simulation in Materials Science and Engineering 18 (2010). [doi:10.1088/0965-0393/18/1/015012](https://doi.org/10.1088/0965-0393/18/1/015012).
- [33] A. K. Mukherjee, An examination of the constitutive equation for elevated temperature plasticity, Materials Science and Engineering: A 322 (2002). [doi:10.1016/S0921-5093\(01\)01115-7](https://doi.org/10.1016/S0921-5093(01)01115-7).
- [34] N. Dowling, S. Kampe, M. Kral, Mechanical Behavior of Materials: Engineering Methods for Deformation, Fracture, and Fatigue, 5th Edition, Pearson Education Limited, 2020.
- [35] R. L. Coble, A model for boundary diffusion controlled creep in polycrystalline materials, Journal of Applied Physics 34 (1963). [doi:10.1063/1.1702656](https://doi.org/10.1063/1.1702656).

- 759 [36] Y. J. Wang, A. Ishii, S. Ogata, Transition of creep mechanism in nanocrystalline metals,
760 Physical Review B - Condensed Matter and Materials Physics 84 (2011). [doi:10.1103/PhysRevB.84.224102](https://doi.org/10.1103/PhysRevB.84.224102).
- 762 [37] D. R. Olander, A. T. Motta, Light Water Reactor Materials Volume I: Fundamentals,
763 American Nuclear Society, 2017.
- 764 [38] A. Y. Kuksin, S. V. Starikov, D. E. Smirnova, V. I. Tseplyaev, The diffusion of point
765 defects in uranium mononitride: Combination of DFT and atomistic simulation with
766 novel potential, Journal of Alloys and Compounds 658 (2016) 385–394. [doi:10.1016/j.jallcom.2015.10.223](https://doi.org/10.1016/j.jallcom.2015.10.223).
- 768 [39] S. L. Hayes, J. K. Thomas, K. L. Peddicord, Material property correlations for uranium
769 mononitride IV. thermodynamic properties, Journal of Nuclear Materials 171 (1990)
770 300–318.
- 771 [40] P. M. Larsen, Revisiting the common neighbour analysis and the centrosymmetry pa-
772 rameter (2020). [arXiv:2003.08879](https://arxiv.org/abs/2003.08879).
- 773 [41] C. L. Kelchner, S. Plimpton, Dislocation nucleation and defect structure during surface
774 indentation, Physical Review B - Condensed Matter and Materials Physics 58 (1998).
775 [doi:10.1103/PhysRevB.58.11085](https://doi.org/10.1103/PhysRevB.58.11085).
- 776 [42] V. Bulatov, W. Cai, Computer Simulations of Dislocations, Oxford University Press,
777 2006.
- 778 [43] A. Stukowski, V. V. Bulatov, A. Arsenlis, Automated identification and indexing of
779 dislocations in crystal interfaces, Modelling and Simulation in Materials Science and
780 Engineering 20 (2012). [doi:10.1088/0965-0393/20/8/085007](https://doi.org/10.1088/0965-0393/20/8/085007).
- 781 [44] W. Cai, W. Nix, Imperfections in Crystalline Solids, 1st Edition, Cambridge University
782 Press, 2016. [doi:10.1017/cbo9781316389508](https://doi.org/10.1017/cbo9781316389508).
- 783 [45] P. Kebinski, D. Wolf, S. R. Phillpot, H. Gleiter, Self-diffusion in high-angle FCC metal
784 grain boundaries by molecular dynamics simulation, Philosophical Magazine A: Physics
785 of Condensed Matter, Structure, Defects and Mechanical Properties 79 (1999). [doi:
786 10.1080/01418619908212021](https://doi.org/10.1080/01418619908212021).
- 787 [46] K. L. Murty, I. Charit, An Introduction to Nuclear Materials, 1st Edition, Wiley-VCH
788 Verlag GmbH & Co. KGaA, 2013.
- 789 [47] V. Yamakov, D. Wolf, M. Salazar, S. R. Phillpot, H. Gleiter, Length-scale effects in
790 the nucleation of extended dislocations in nanocrystalline Al by molecular-dynamics
791 simulation, Acta Materialia 49 (2001). [doi:10.1016/S1359-6454\(01\)00167-7](https://doi.org/10.1016/S1359-6454(01)00167-7).
- 792 [48] R. S. Gordon, Ambipolar diffusion and its application to diffusion creep, Materials
793 Science Research 9 (1974). [doi:10.1007/978-1-4684-3150-6_30](https://doi.org/10.1007/978-1-4684-3150-6_30).

- 794 [49] M. Kizilyalli, J. Corish, R. Metselaar, Definitions of terms for diffusion in the solid state,
795 Pure and Applied Chemistry 71 (1999). [doi:10.1351/pac199971071307](https://doi.org/10.1351/pac199971071307).
- 796 [50] E. W. Hart, On the role of dislocations in bulk diffusion, Acta Metallurgica 5 (1957).
797 [doi:10.1016/0001-6160\(57\)90127-X](https://doi.org/10.1016/0001-6160(57)90127-X).
- 798 [51] A. A. Riet, J. A. V. Orman, D. J. Lacks, A molecular dynamics study of grain boundary
799 diffusion in mgo, Geochimica et Cosmochimica Acta 292 (2021). [doi:10.1016/j.gca.2020.09.012](https://doi.org/10.1016/j.gca.2020.09.012).
- 800 [52] T. Arima, K. Yoshida, K. Idemitsu, Y. Inagaki, I. Sato, Molecular dynamics analysis
801 of diffusion of uranium and oxygen ions in uranium dioxide, IOP Conference Series:
802 Materials Science and Engineering 9 (2010).
- 803 [53] D. Prokoshkina, V. A. Esin, G. Wilde, S. V. Divinski, Grain boundary width, energy
804 and self-diffusion in nickel: Effect of material purity, Acta Materialia 61 (2013). [doi:10.1016/j.actamat.2013.05.010](https://doi.org/10.1016/j.actamat.2013.05.010).
- 805 [54] A. Cheniour, M. R. Tonks, B. Gong, T. Yao, L. He, J. M. Harp, B. Beeler, Y. Zhang,
806 J. Lian, Development of a grain growth model for U₃Si₂ using experimental data, phase
807 field simulation and molecular dynamics, Journal of Nuclear Materials 532 (2020). [doi:10.1016/j.jnucmat.2020.152069](https://doi.org/10.1016/j.jnucmat.2020.152069).
- 808 [55] Z. Zeng, Y. Pan, X. Chen, C. Zhang, C. Yin, S. Gao, Y. Zhou, J. Zhang, X. He, C. Yuan,
809 Three-dimensional modeling of thermal-mechanical behavior of accident tolerant fuels,
810 Frontiers in Energy Research 9 (2021). [doi:10.3389/fenrg.2021.636502](https://doi.org/10.3389/fenrg.2021.636502).
- 811 [56] E. W. Weisstein, [Truncated octahedron](#), MathWorld: A Wolfram Web Resource.
812 URL <https://mathworld.wolfram.com/TruncatedOctahedron.html>